Kinetics of zeolite-catalyzed heptane hydroisomerization and hydrocracking with CBMC-modeled adsorption terms

Zeolite Beta as a large pore base case

Agarwal, U.; Rigutto, M.S.; Zuidema, E.; Jansen, A.P.J.; Poursaeidesfahani, A.; Sharma, S.; Dubbeldam, D.; Vlugt, T.J.H.

DOI
10.1016/j.jcat.2022.09.026

Publication date
2022

Document Version
Final published version

Published in
Journal of Catalysis

License
CC BY-NC-ND

Journal of Catalysis 415 (2022) 37–50

Contents lists available at ScienceDirect

Journal of Catalysis

journal homepage: www.elsevier.com/locate/jcat

Kinetics of zeolite-catalyzed heptane hydroisomerization and hydrocracking with CBMC-modeled adsorption terms: Zeolite Beta as a large pore base case

Umang Agarwal [a], Marcello S. Rigutto [a,*], Erik Zuidema [a], A.P.J. Jansen [b], Ali Poursaeidesfahani [c], Shrinjay Sharma [c], David Dubbeldam [d], Thijs J.H. Vlugt [c]

[a] Shell Global Solutions International B.V., P.O. Box 38000, 1030 BN Amsterdam, The Netherlands
[b] Shell India Markets Private Limited, Kundanahalli Main Road, Bangalore 560048, Karnataka, India
[c] Engineering Thermodynamics, Process & Energy Department, Faculty of Mechanical, Maritime and Materials Engineering, Delft University of Technology, Leeghwaterstraat 39, 2628CB Delft, The Netherlands
[d] Van 't Hoff Institute of Molecular Sciences, University of Amsterdam, Science Park 904, 1098XH Amsterdam, The Netherlands

ARTICLE INFO

Article history:
Received 29 July 2022
Revised 10 September 2022
Accepted 23 September 2022
Available online 2 October 2022

Keywords:
Shape selectivity
Zeolite catalysis
Bifunctional catalysis
Hydroisomerization
Hydrocracking
Molecular simulation

ABSTRACT

A reactor model that deconvolutes thermodynamics of adsorption of hydrocarbon in the pores of zeolite Beta, obtained by Configurational-bias Monte Carlo simulations, from intrinsic, intraporous kinetics of hydroisomerization and hydrocracking reactions, provides a good quantitative description of all significant reactions in the kinetic network for interconversion and cracking of different heptane isomers. Activation enthalpies obtained for intraporous reactions follow the expected order according to the carbenium ion formalism:

methyl shift< ethyl shift < isom(B) ∼ crack(B2) < crack(B1) < crack(C) ∼ crack(D) < crack(E)

and apparently within each isomerization class, in terms of carbenium ions formally involved:

sec → *tert* < *sec* → *sec* ∼ *tert* → *tert* < *tert* → *sec*.

except for the ethyl shift reaction forming 3-ethylpentane. Cracking happens primarily through 2,4-dimethylpentane (type B2), regardless of the initial reactant. The model can be subsequently used to separate the effect of pore structure on selective adsorption and on intraporous reaction kinetics. Zeolite Beta will serve as a base case for a comparison of different zeolite structures.

1. Introduction

The chemistry of zeolite-catalyzed hydroisomerization and hydrocracking of alkanes enables economically important processes for the production of fuels, lubricants and petrochemicals [1], but also presents an extremely useful study case for shape-selective catalysis [2]. Although it is better understood than most zeolite-catalyzed reactions, there is also still considerable debate as to how shape selectivity operates exactly. Selective adsorption (most common form of "reactant selectivity") [2], steric constraint on intrinsic rates ("transition state selectivity") [3,4] and specific diffusion constraints (most common form of "product selectivity") [2,3,5–7] are assigned varying contributions based, in most cases, on qualitative arguments. A more thorough quantitative understanding of a detailed kinetic network could make it possible to disentangle these contributions and, *in casu*, clarify how the zeolite pore structure specifically influences adsorption terms and intrinsic kinetic terms in individual reaction rates, and, in some cases, impedes diffusion of specific products.

This paper aims to provide such a quantitative description of the kinetic network of hydroisomerization and hydrocracking of heptanes over zeolite Beta (assisted by palladium), using different heptane isomers as starting compounds. Zeolite Beta was chosen as the first target zeolite for this study after it was verified in preliminary studies on adsorption thermodynamics that its structure does not differentiate strongly among heptane isomers (*i.e.*, displaying relatively weak shape selectivity), presenting a case in which contributions from selective adsorption and intrinsic kinetics (in a limited sense explained further below) would be more easily separated. The heptanes hydroisomerization/hydrocracking case is informative in that its reactions are all monomolecular, while it lacks the fast type A cracking of α,α,γ-trisubstituted isomers only available for carbon numbers of 8 and higher [8],

* Corresponding author.
E-mail address: marcello.rigutto@shell.com (M.S. Rigutto).

https://doi.org/10.1016/j.jcat.2022.09.026
0021-9517/

allowing more accurate estimates of the slower cracking paths. Also, in our experience, within a wide range of catalyst activities, zeolite crystal sizes, etc., heptanes hydroisomerization/hydrocracking displays no signs of diffusion limitation for most zeolite materials, except for certain medium or small-pore materials with cages or pore intersections, such as ZSM-5 and ZSM-11 [6]. In these structures especially dibranched molecules experience high free energy barriers for diffusion between intersections, leading to enhanced cracking and low isomerization yields.

As we establish the base case kinetics for zeolite Beta as a weak shape selectivity case here, an aim in subsequent papers will be to establish to which extent different selectivities displayed by other structures considered to be more shape selective, such as ZSM-12, ZSM-23, and ZSM-48, can be explained by different adsorption thermodynamics only, or also require different intrinsic rates.

Quantitative single event microkinetic descriptions have previously been constructed for the hydroisomerization and hydrocracking of C8 to C12 alkanes on Pt/H-US-Y [9,10], of *n*-hexadecane [11] and *n*-heptane [12] on Pt/H-beta zeolite and of *n*-decane on Pt/H-ZSM-22 [13]. For modeling our heptane datasets, we chose not to start from e.g. the C8 single event model per se (*mutatis mutandis* for C7) but rather to explicitly consider all relevant *alkane* interconversions in the C7 network without prior lumping. In this way, the responses of individual intrinsic rates to zeolite structure are kept probeable. One simplification we applied was to make other steps in the bifunctional scheme ((de) hydrogenation, reactions of alkenes) implicit (*i.e.,* collapsed into the alkane interconversions), as is schematically shown in Fig. 1. This simplification avoids assumptions on the intermediates involved and their energies, but further interpretation of the fitted barriers of course does require such assumptions, which we will explicate in the discussion. As will be shown below, the model yields quantitative information for activation barriers of all the significant reaction pathways which aligns well with expectations of carbenium ion chemistry. Further analysis with the model help determine the dominant isomerization and cracking pathways for various heptane isomers.

2. Experimental methods, procedures, and model equations

2.1. Materials and catalyst sample preparation

Zeolite Beta with Si/Al = 50 mol/mol, a BET surface area of 700 m^2/g and a crystal size of approximately 400 nm was obtained from Zeolyst International. The powder was loaded with 0.4 wt% Pd via ion exchange with a solution of an appropriate concentration of $Pd(NH_3)_4(NO_3)_2$. The resulting materials were dried at 393 K for 2 h and subsequently calcined in air at 523 K (50 K/h ramp rate, 2 h hold time). Pd dispersion by hydrogen chemisorption was found to be H/Pd = 0.32 mol/mol, corresponding to a particle size of 3.5 nm (assuming hemispherical Pd particles).

n-Heptane (Merck, 99%), 2-methylhexane (abcr GmbH, 99%) and 2,2-dimethylpentane (abcr GmbH, 96%) were used as purchased.

2.2. Catalytic activity measurements

Hydroconversion of *n*-heptane and isoheptanes was carried out on Pd-loaded zeolite Beta as described previously [14]. Pd was used in these tests as Pt often contributes significantly to hydrogenolysis reactions, especially at temperatures above 573 K (see e.g. [15]). The catalysts were pressed and sieved to a size fraction (177–420 μm) and reduced prior to reaction in flowing hydrogen heating with 5 K/min to 713 K at 30 bar. Hydroconversion was carried out in a flow setup at 30 barg, varying the amount of catalyst from 100 to 300 mg to vary space velocity and using a H_2 flow of 25 ml/min subsequently saturated with the feed (iso)alkane at 383 K and reaction pressure, yielding H_2/hydrocarbon ratios of 14.2 (2,2-dimethylpentane), 19.2 (2-methylhexane) or 24.3 mol/mol (*n*-heptane). The reaction temperature was varied between 713 K and 473 K, and products were analyzed by online GC (runs from 480 K to 625 K are used in our modeling scheme as those involve product streams with multibranched isomers and cracking products).

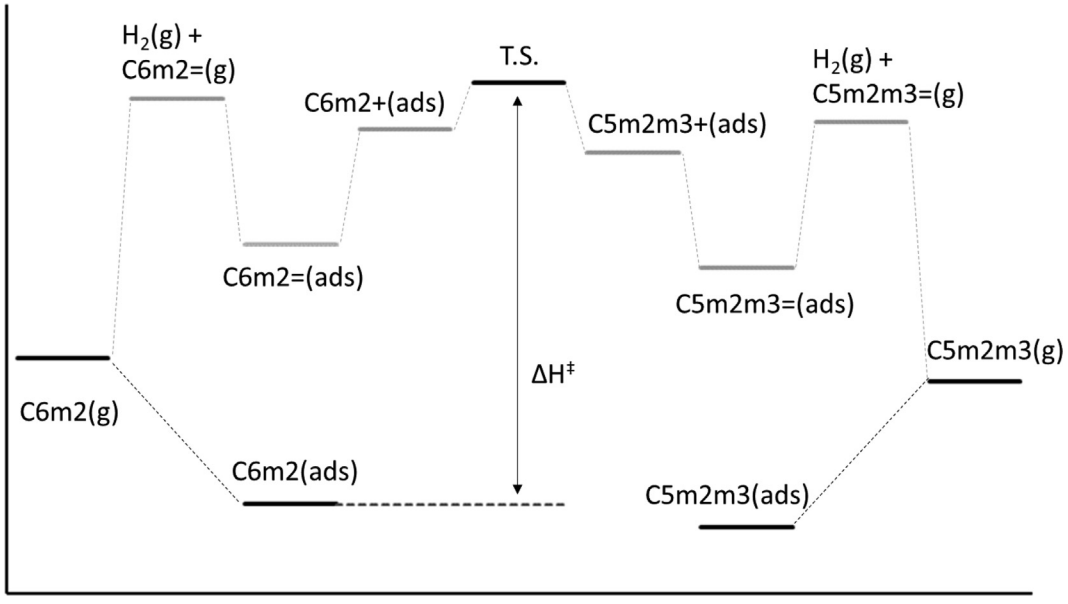

Fig. 1. Schematic enthalpy diagram of the reaction from 2-methylhexane (C6m2) to 2,3-dimethylpentane (C5m2m3), as an example. The activation enthalpies $\Delta H^{\ddagger}$ fitted in this work are not those of elementary steps but rather of the interconversion of alkanes adsorbed in the zeolite pores, as illustrated. C6m2= is e.g. 2-methyl-2-hexene, C6m2+ is e.g. 2-methylhex-3-enium, C2m2m3+ is e.g. 2,3-dimethylpent-4-enium, C5m2m3= is e.g. 2,3-dimethyl-2-hexene.

2.3. Adsorption isotherms

Adsorption isotherms and free energy profiles of heptane isomers in all-silica zeolite Beta were computed using force field-based Monte Carlo (MC) simulations at temperatures ranging from 480 K to 660 K. Isotherms follow from simulations in the grand-canonical ensemble. The RASPA software package was used for all MC simulations [16,17]. The following types of trial moves were used: translations, rotations, random reinsertions, partial and full regrowth using the Configurational-Bias Monte Carlo (CBMC) technique, and exchanges with the reservoir (insertions and deletions) using the CBMC technique [18–21]. For more simulation details, the reader is referred to Refs. [18,22,23]. Heptane isomers were modeled using the united-atom TraPPE force field which contains intra- and intermolecular Lennard-Jones interactions, intramolecular bond-bending and torsion interactions, and fixed C-C bonds [24,25]. The TraPPE-zeo force field was used to model the interactions between the hydrocarbons and the zeolite [26]. Lennard-Jones interactions were truncated and shifted at 12 Å and no tail corrections were applied. The simulation box consists of $2 \times 2 \times 1$ rigid unit cells for BEA-type zeolite with periodic boundary conditions (Fig. 2, right). All-silica zeolite structures were taken from the IZA database [27] and were considered as rigid [28]. Widom's test particle method was used [29] to compute the Henry coefficients. The enthalpy of adsorption at infinite dilution was calculated from the energy difference of a single molecule inside and outside the framework in the NVT ensemble [30].

2.4. Reaction network and reactor model

It is well known that hydroconversion of alkanes in bifunctional metal zeolite catalysts occurs via dehydrogenation/hydrogenation at metal sites and isomerization/cracking reactions at zeolitic Brønsted acid sites [8,31]. With sufficient activity from the metal, dehydrogenation/hydrogenation is fast relative to the acid-catalyzed reactions and (iso)alkenes can be assumed to be present at (low) equilibrium levels relative to the corresponding (iso)alkanes [10,32]. It then is the dilute (iso)alkenes that react at zeolitic Brønsted acid sites to undergo isomerization or scission reactions, followed by rehydrogenation of the products. Although in many cases carbenium ions can be thought of as metastable species rather than stable intermediates in zeolite chemistry [33], elementary reactions are still usefully conceived and discussed as carbenium ion reactions [8,12,34,35], as we will also do here.

In our reaction model, we simulate all possible isomerization and cracking reaction pathways [31] which result in changes in

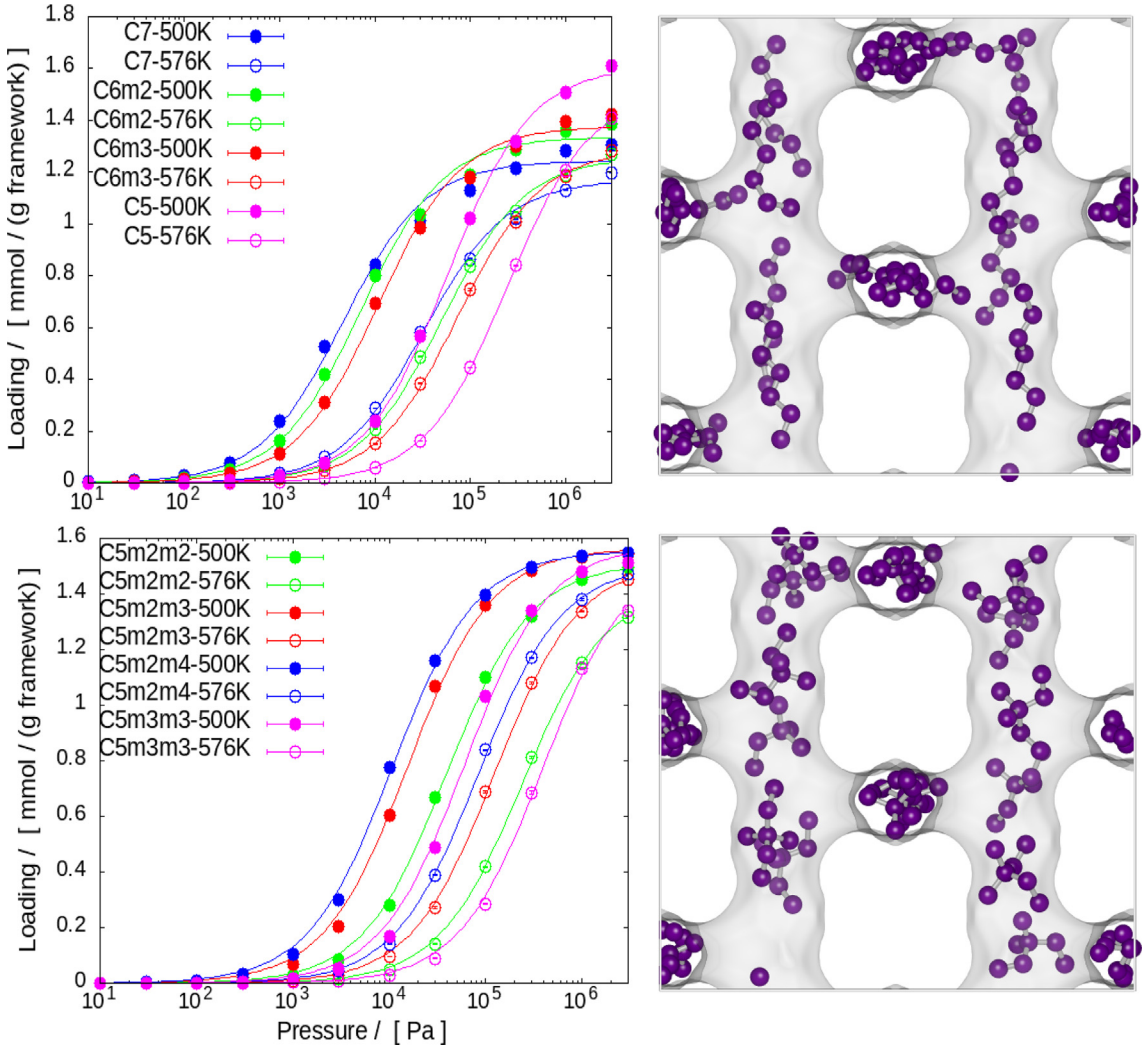

Fig. 2. Left: Adsorption isotherms obtained from Configuration-Bias Monte Carlo simulations of mono-methyl isomers and linear alkanes (top) and dimethyl isomers (bottom) at 500 K and 576 K. Right: Snapshots of *n*-heptane (top) and 3,3-dimethylpentane (bottom), absorbed in the pores of zeolite Beta as observed in typical simulations, both at high loadings, achieved at 10^6 Pa and 500 K.

carbon skeleton along with the adsorption thermodynamics of alkanes in zeolite Beta calculated using Configuration-Bias Monte Carlo simulations. We consider reaction pathways based on mechanisms of rearrangements of alkylcarbenium ions [36,37]. All possible secondary and tertiary carbenium ion intermediates that can be formed by protonation of alkenes corresponding to various heptane isomers are considered for type A and type B isomerization reactions [38,39]. Type A isomerization reactions lead to shifting of alkyl groups through a corner-protonated cyclopropane (PCP) transition state to form isomeric alkanes with an equal number of branches. In type B isomerization, the branching degree changes, which involves a higher barrier [40–42], due to an asymmetric transition state described by Sandbeck et al. [43] as closed primary meso-PCP and by Rey et al. as an asymmetric edge-protonated CP [44,45].

All possible type A and type B isomerization pathways are considered. An illustration of reactions involving 2,3-dimethylpentane is shown in Fig. 3 (similar isomerization pathways are considered for each isomer and the resulting reaction network is drawn in Fig. 4). In case there are type A as well as type B isomerization reactions feasible for interconversion of two isomers, the reaction network marks them as type A due to lower activation energies for these reactions (however the net reaction rate would be due to both type of reactions occurring in parallel). Only isomerization pathways which result in formation of a primary carbenium ion are not included in the reaction network as these reactions would entail a very high activation energy [8]. We use a condensed notation to represent the various isomers and cracking products of *n*-heptane in our reaction scheme instead of their IUPAC name. This scheme starts with the C backbone length followed by side groups and their positions, e.g. 2,3-dimethyl-pentane is represented as C5m2m3, 3-ethyl-pentane is represented as C5e3.

Cracking reactions proceed through β-scission of carbenium ions. The rates of various cracking pathways are linked to the stability of the carbenium ions involved in the reaction. Typically, four types of reactions are dominant in cracking of C_8^+ molecules: type A (tertiary to tertiary carbocation), type B1 (secondary to tertiary carbocation), type B2 (tertiary to secondary carbocation) and type C (secondary to secondary carbocation) [8,46]. For smaller alkanes Type D (secondary to primary carbocation or vice versa) and type E (tertiary to primary carbocation or vice versa) [47] are also considered, however, their rate constants are quite low due to the relatively unstable primary carbocation formation. For heptane isomers, Type A hydrocracking is not feasible as it requires three branches in α,γ,γ positions, hence Type B1, B2 and C cracking mechanisms are the most prominent routes of cracking as illustrated in Fig. 3. Some of the type D/E cracking pathways are also included in our reaction scheme to account for formation of small amounts of pentane and isopentane products by cracking of 3-ethylpentane and 3,3-dimethylpentane, respectively. Other type D and E cracking reactions are included for completeness though they are expected to contribute minimally to the overall reaction network.

2.4.1. Rate equations

The loading of various heptane isomers and lower carbon number cracking products adsorbed on zeolite Beta across the catalyst bed are computed using a mixed Langmuir adsorption isotherm with parameters derived from single-component Langmuir fits to the CBMC calculated isotherms. This enables use of rate expressions in terms of intraporous (iso)alkane concentrations. A comparison between mixed Langmuir and IAST isotherms was carried out at relevant temperatures and partial pressures to ensure sufficient accuracy of the mixed Langmuir approximation, essentially because partial pressures of the various components remain low enough to avoid significant competitive effects (see supplementary information). Since the full reaction scheme involving all possible (iso)alkene intermediates and their adsorption is too complex to model, our assumption that the reactions have first order kinetics in intraporous (iso)alkane concentration is a necessary simplification, whose accuracy can be judged from the quality of the model fits. It is only the *interpretation* of the resulting kinetic parameters in terms of elementary steps that then requires further assumptions, *viz.* that enthalpies and free energies of adsorption of (iso) alkene, alkoxide and carbenium ion intermediates (see Fig. 1) vary as a function of the carbon backbone (and resulting molecular shape) in the same way as those of the corresponding (iso)alkanes. In that sense, rate constants and activation energies estimated in this paper are still composite numbers rather than true single event kinetic parameters, however, they represent intrinsic kinetics in the limited sense that they allow intraporous reaction kinetics to be considered separately from selective adsorption effects.

According to Eyring transition state theory [48], the rate constant k for a given activated reaction is:

$$k = \frac{k_B T}{h} e^{\Delta S^{\ddagger}/R} e^{-\Delta H^{\ddagger}/RT} \tag{1}$$

Since most of the isomerization reactions involve formation of a (meso-)protonated cyclopropane transition state, to reduce number of fitting parameters we use only single independent parameters for calculating the contribution due to change of entropy ($e^{\Delta S^{\ddagger}/R}$). Similarly, for cracking reactions a single parameter is used for all cracking reactions involving a C_7 carbocation and another parameter for reactions involving a C_5 carbocation. For activation enthalpies ($\Delta H^{\ddagger}$) each isomerization and cracking reaction (13 isomerization and 11 cracking reactions) has a unique fitting parameter which are determined together with the 3 different $e^{\Delta S^{\ddagger}/R}$ prefactors by minimizing an objective function which compares the concentrations of these isomers formed at different gas hourly space velocities and temperatures (as described in the section of Experimental Methods). For reverse isomerization reactions we can write,

$$k_{-1} = \frac{k_B T}{h} e^{-\Delta G_{-1}^{\mathrm{ads}\ddagger}/RT} \tag{2}$$

where $\Delta G_{-1}^{\mathrm{ads}\ddagger}$ is the change in Gibbs free energy for transition from product in adsorbed phase to activated complex:

$$\begin{aligned}\Delta G_{-1}^{\mathrm{ads}\ddagger} &= G_{\ddagger}^{\mathrm{ads}} - G_{\mathrm{product}}^{\mathrm{ads}} \\ &= G_{\ddagger}^{\mathrm{ads}} - G_{\mathrm{reactant}}^{\mathrm{ads}} - (G_{\mathrm{product}}^{\mathrm{ads}} - G_{\mathrm{reactant}}^{\mathrm{ads}}) \\ &= \Delta G^{\mathrm{ads}\ddagger} - \Delta G_{\mathrm{R-P}}^{\mathrm{ads}}\end{aligned} \tag{3}$$

where, $\Delta G_{\mathrm{R-P}}^{\mathrm{ads}}$ is the difference in Gibbs free energy of formation (in adsorbed state) of reactant and product isomers and $\Delta G^{\mathrm{ads}\ddagger}$ is the change in Gibbs free energy for transition from reactants in adsorbed phase to activated complex. Based on Equation (3), the rate constant for reverse reaction can be determined by computing the difference in Gibbs free energy of formation (in adsorbed state) of reactant and product isomers and the forward rate constant (directly related to $\Delta G^{\mathrm{ads}\ddagger}$ as per equation (1)) determined using the fitted parameters. This limits our fitting parameters significantly and imposes thermodynamic constraints on the reaction network.

For determining the difference in Gibbs free energy for isomers in adsorbed state we use the values for the Gibbs free energies of formation ΔG_F° of heptane isomers in gaseous form as reported by Scott [49] at temperatures of interest and use the equilibrium constants for adsorption (from Langmuir isotherms) at the same temperatures for calculating the difference in Gibbs free energy for adsorption of reactant and product. This leads to

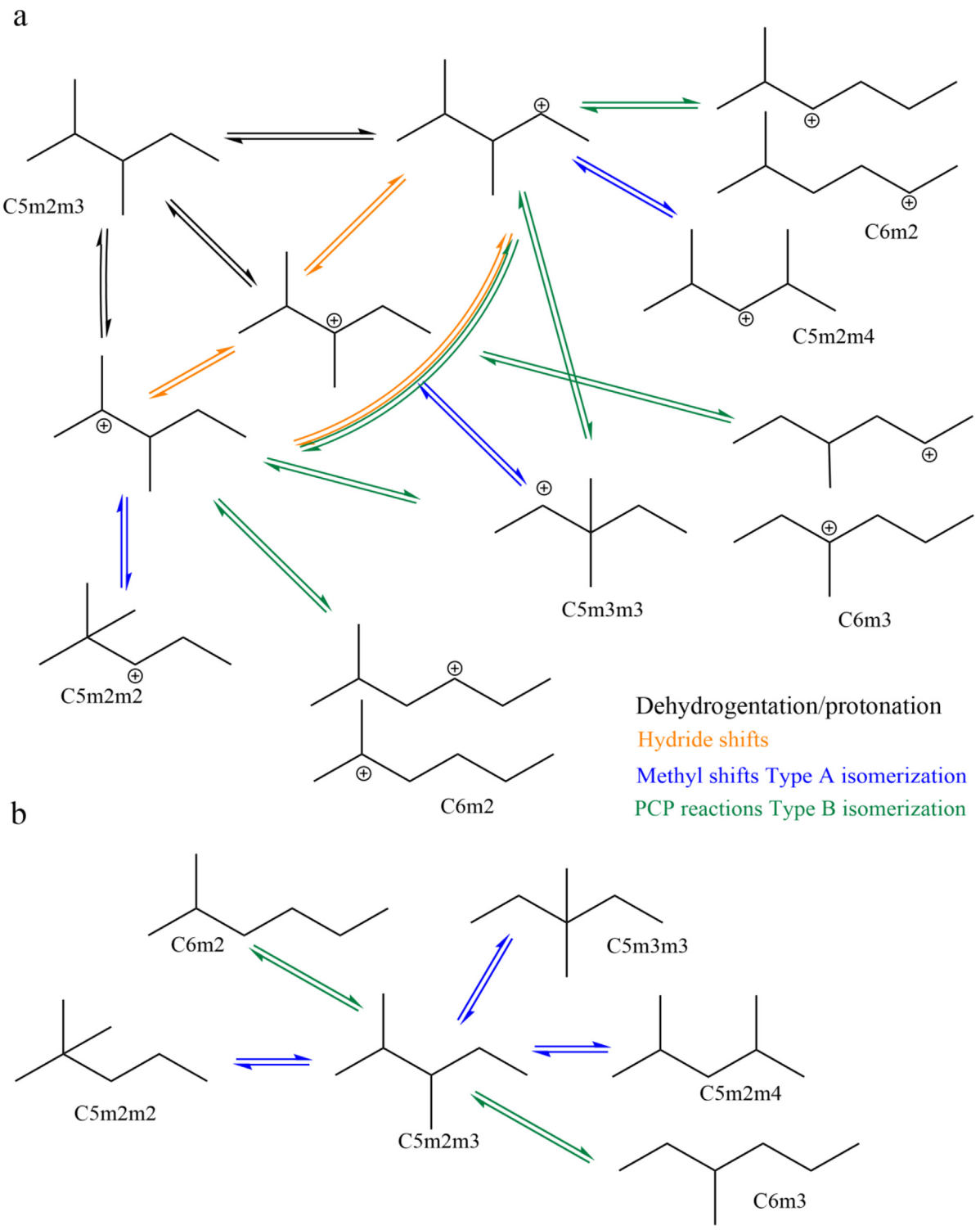

Fig. 3. (a) Illustration of all possible isomerization pathways for 2,3-dimethyl-pentane with dehydrogenation and protonation followed by backbone isomerization of type A (methyl or ethyl shift, blue arrows) or type B (branching isomerization, green arrows). (b) Reaction pathways used to model isomerization reactions associated with 2,3-dimethyl-pentane in our reaction network. (For interpretation of the references to colour in this figure legend, the reader is referred to the web version of this article.)

$$\Delta G^{ads}_{R-P} = (\Delta G^{o}_{F,P} + \Delta G^{ads}_{P}) - (\Delta G^{o}_{F,R} + \Delta G^{ads}_{R}) \quad (4)$$

Where, $\Delta G^{o}_{F,P}$ and $\Delta G^{o}_{F,R}$ are the Gibbs free energy of formation for the product and reactants respectively, and ΔG^{ads}_{P} and ΔG^{ads}_{R} are the free energy of adsorption for product and reactant molecules respectively. The Gibbs free energy of adsorption for isomer i of heptane is related to the equilibrium constants for adsorption (Langmuir isotherms) by

$$\Delta G^{ads}_{i} = -RTln(K^{i}_{eq}) \quad (5)$$

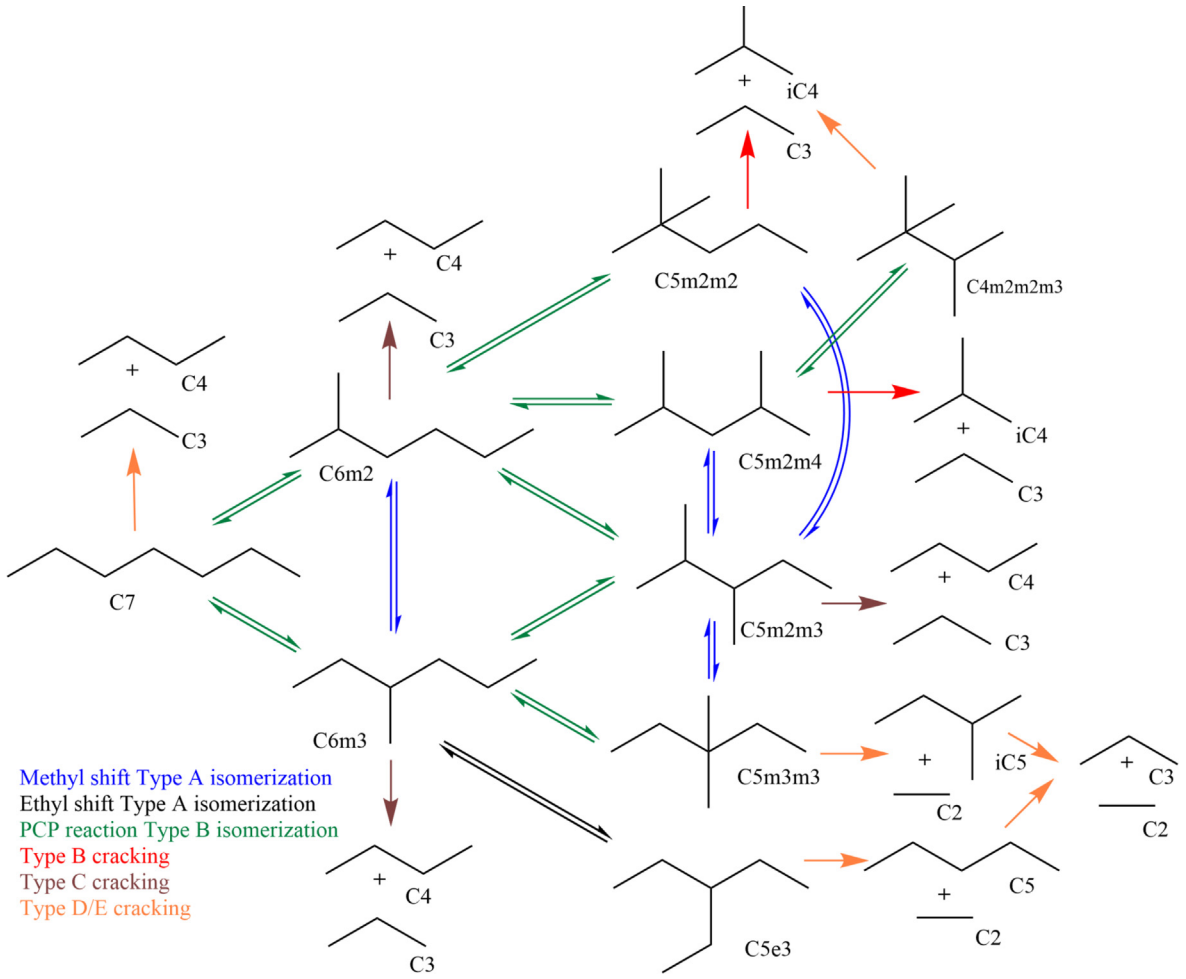

Fig. 4. Complete kinetic reaction network of (iso)alkane hydroconversion interconversions and hydrocracking reactions based on considering all possible isomerization pathways as illustrated in Fig. 3. Blue arrows indicate reversible Type A isomerization reactions; Green arrows indicate reversible Type B isomerization reactions. Red arrows indicate irreversible type B cracking reactions, brown arrows indicate irreversible type C cracking and orange arrows indicate irreversible type D/E reactions which occur at very low rates. (For interpretation of the references to colour in this figure legend, the reader is referred to the web version of this article.)

Using Equation (5) in Equation (4) and (3) we find

$$\Delta G_{-1}^{\mathrm{ads}^{\ddagger}} = \Delta G^{\mathrm{ads}^{\ddagger}} - \left(\Delta G^{\mathrm{o}}_{\mathrm{R-P}} - RTln\left(\frac{K^{\mathrm{P}}_{\mathrm{eq}}}{K^{\mathrm{R}}_{\mathrm{eq}}}\right)\right) \tag{6}$$

and using Equation (6) in Equation (2) and substituting the forward rate constant equation from Equation (1) leads to

$$k_{-1} = \frac{k_B T}{h} e^{-\left(\Delta G^{\mathrm{ads}^{\ddagger}} - \left(\Delta G^{\mathrm{o}}_{\mathrm{R-P}} - RTln\left(\frac{K^{\mathrm{P}}_{\mathrm{eq}}}{K^{\mathrm{R}}_{\mathrm{eq}}}\right)\right)\right)/RT}$$

$$= k\frac{K^{\mathrm{R}}_{\mathrm{eq}}}{K^{\mathrm{P}}_{\mathrm{eq}}} e^{\Delta G^{\mathrm{o}}_{\mathrm{R-P}}/RT} \tag{7}$$

Hence, the reverse rate constant k_{-1} for isomerization reactions can be calculated using the forward rate constant k. In this equation, $K^{\mathrm{R}}_{\mathrm{eq}}$ and $K^{\mathrm{P}}_{\mathrm{eq}}$ are equilibrium constants for adsorption of reactant and product isomers respectively and $\Delta G^{\mathrm{o}}_{\mathrm{R-P}}$ is difference in free energy of formation of product and reactant isomers obtained from Scott [49] at temperatures of interest.

2.4.2. Reactor model and optimization

The tubular fixed bed flow reactor is modeled using a one-dimensional finite difference scheme. Uniform isothermal plug flow with constant gas hourly space velocity is assumed to model the experimental run. Gas phase partial pressures and adsorbed phase loading of each component is calculated at each node in the axial direction with the inlet gas composition used as a boundary condition. The reactor model requires mass balance of gas phase components which are in equilibrium with the adsorbed phase as transport of components happens in gas phase while the reaction happens in adsorbed phase. Assuming steady state isothermal conditions, the mass balance can be written as

$$\frac{dn_{i,\mathrm{ads}}}{dW} = R_{i,\mathrm{ads}} \tag{8}$$

where $R_{i,\mathrm{ads}}$ is the net rate of production (or consumption) of component i in adsorbed phase, $n_{i,\mathrm{ads}}$ is molar concentration of component i in adsorbed phase, and W is weight of catalyst (which is evenly divided in each node in the axial direction). The change in concentration of each component in adsorbed phase is then used to calculate the corresponding change in partial pressure in gas phase, assuming ideal gas behavior

$$\Delta p_{i,g} = \frac{RT_{\mathrm{exp}}\Delta n_{i,\mathrm{ads}}}{V} \tag{9}$$

where $\Delta p_{i,g}$ is the change in partial pressure of component i in gas phase, V is the pore volume of catalyst bed, R is the universal gas constant, and T_{exp} is the experimental temperature. The partial pressures of each component are updated at current node and used

to calculate the equilibrium loading in next node which determine rates of reactions in next node. Corresponding to the experimental runs, reactor simulations were conducted for 5 different sets of gas hourly space velocity (GHSV) from 72.45 Nml/g/min (300 mg catalyst) to 244.4 Nml/g/min (100 mg catalyst) and 12 different temperature conditions ranging from 473 to 623 K. Three different datasets were used with different heptane isomer feeds: *n*-heptane, 2-methylhexane, and 2,2-dimethylpentane. To allow for some run-to-run variability of the catalytic results a fitting parameter was used as pre-factor multiplier for all isomerization and cracking reactions for the 2-methylhexane simulation and another fitting multiplier for the 2,2-dimethylpentane simulation. For optimizing these 29 fitting parameters (24 enthalpies of activation, 3 pre-factors for entropic contributions and 2 activity multipliers) we used the Genetic Algorithm GA toolbox of MATLAB™. The optimization objective function was defined using a mean normalized sum of squared residuals (MNSSR) which averages the squared difference between the experimental and simulated mole fraction of all components (for all runs) divided by the range of experimental mole fractions for each component. This normalization equalizes the contribution from all components, even if they are formed in smaller fraction compared to other components. The objective function is defined as:

$$MNSSR = \frac{\sum_{j=0}^{N}\sum_{i=0}^{n}\left(\frac{x_{i,j}^{\text{model}} - x_{i,j}^{\text{experiment}}}{x_{i,\max_j}^{\text{experiment}} - x_{i,\min_j}^{\text{experiment}}}\right)^2}{N \times n - p}$$

$x_{i,j}^{\text{model}}$ and $x_{i,j}^{\text{experiment}}$ are the mole fractions of component *i* for run *j* calculated using the model and observed in experiment respectively. *N* is the total number of experiments conducted at different temperature and gas hourly space velocity conditions, *n* is the number of components formed in our reaction network and *p* is the number of fitted parameters. The final objective function used in global minimization was an average of MNSSR values computed for the three sets of models and experiments conducted with different heptane isomer feeds (*n*-heptane, 2-methylhexane and 2,2-dimethylpentane feed datasets respectively). For setting up the global optimization problem in the MATLAB™ GA toolbox various combination of population sizes (ranging from 10,000 to 500000) and number of generations (50–200) were tested and the final fitness values were compared to select an optimal population size of 400,000 and 100 generations. The range of various fitting parameters is also modified in multiple iterations of global optimization simulations to ensure no optimized fits includes any boundary values and the combination resulting in lowest objective function values are used. The optimized parameter set is averaged from 10 different simulations involving different range and starting conditions. The global optimization runs were carried using the MATLAB parallel computing toolbox with 40 threads on high performance computing nodes with two Intel® Xeon® Gold 6248 processors (27.5 M Cache and 2.5 GHz) and 380 GB RAM.

3. Results and discussion

3.1. Adsorption isotherms

In Fig. 2, (left) we plot the adsorption isotherms for monomethyl and linear isomers of heptane and *n*-pentane (cracking product) in the top left frame and all dimethyl isomers in bottom left frame at two temperatures (500 K and 576 K). It can be observed that amongst all dimethylpentanes, 2,4-dimethylpentane has the highest loadings at all pressures. Amongst the monomethyl and linear isomers, *n*-heptane has higher loading at lower pressures while *n*-pentane has higher loading at higher pressures due to its smaller C backbone. Similarly, the dimethylpentane isomers (2,4-dimethylpentane) also have slightly higher loadings compared to *n*-heptane at higher pressure (larger than 105 Pa) due to their shorter backbones.

Table 1 shows Henry coefficients and enthalpies of adsorption at infinite dilution for C7 isomers adsorbed in the pores of zeolite Beta. It is interesting to note the significantly lower exothermicity of adsorption of geminal dimethyl isomers in this structure compared to the other C7 isomers, since not all groups around a quaternary carbon atom can optimally interact with the pore wall in each configuration.

3.2. Model parameter optimization

The global optimization run finds optimized parameters which minimizes the difference between experimental product compositions from hydroconversion experiments and simulated compositions for all three datasets, *viz.* with *n*-heptane, 2-methylhexane and 2,2-dimethylpentane feeds at 5 space velocities for each feed, using the proposed reactor model with detailed reaction network. It first turned out that incorporating the 2,2-dimethylpentane feed results caused some skewing in the fits that were most easily corrected by assuming that, somehow, the overall catalyst activity was lower for this feed than for the other feeds, without changing other parameters in the network. Hence we found it necessary to introduce a single activity multiplier for all rate constants for each different feed, that only in the case of the 2,2-dimethylpentane feed was found to deviate significantly from 1. The simplest explanation for this observation would be that 2,2-dimethylpentane contained a feed impurity acting as inhibitor.

The fitted enthalpies of activation, pre-factors for entropic contribution of transition to activated state and overall activity multipliers per run are tabulated in Tables 2 and 3, and the comparison between simulated data and experimental data is presented in Figs. 5-7. The fitted activation enthalpies follow trends consistent with the carbocation formalism for hydroconversion of alkanes. Type A isomerization reactions have the lowest activation enthalpies between 161 and 170 kJ/mol. The barrier for isomerization to a geminal dimethyl isomer (C5m2m3 to C5m3m3) is at 167 kJ/mol towards the high end of this range, which could be due to the

Table 1
Henry coefficients and enthalpies of adsorption at infinite dilution for C7 isomers adsorbed inside zeolite Beta.

C7 Isomers	at 500 K		at 576 K	
	Henry Coefficient [10^{-6} mol/kg/Pa]	Enthalpy of Adsorption [kJ/mol]	Henry Coefficient [10^{-6} mol/kg/Pa]	Enthalpy of Adsorption [kJ/mol]
C7	235.5 ± 1.0	−62.74 ± 0.21	32.52 ± 0.12	−62.47 ± 0.35
C6m2	152.3 ± 0.4	−61.78 ± 0.19	21.57 ± 0.08	−61.47 ± 0.22
C6m3	107.1 ± 0.9	−61.31 ± 0.26	15.52 ± 0.09	−60.87 ± 0.19
C5m2m2	25.8 ± 0.2	−54.73 ± 0.24	4.59 ± 0.04	−54.21 ± 0.29
C5m2m3	63.1 ± 0.6	−60.81 ± 0.36	9.34 ± 0.06	−60.12 ± 0.27
C5m2m4	97.2 ± 0.3	−61.06 ± 0.20	1.42 ± 0.08	−60.52 ± 0.20
C5m3m3	16.1 ± 0.1	−53.80 ± 0.30	2.94 ± 0.02	−53.13 ± 0.22

Table 2
Fitted kinetic constants (change in enthalpy for activated transition state) optimized over all datasets including runs for *n*-heptane, 2-methylhexane and 2,2-dimethylpentane hydroconversion over zeolite BEA.

Reaction	Reaction type	Activation Enthalpy $\Delta H^{\ddagger}$ (kJ/mol)
C5m2m2 ⇌ C5m2m3	isom A	161.6
	sec → *tert*	(165.8)[a]
C5m2m3 ⇌ C5m2m4	isom A	161.9
	sec → *sec*	
C6m2 ⇌ C6m3	isom A	163.6
	sec → *sec*	
C5m2m3 ⇌ C5m3m3	isom A	167.2
	tert → *sec*	
C6m3 ⇌ C5e3	isom A	170.7
	sec → *sec*	
	ethyl shift	
C6m3 ⇌ C5m2m3	isom B	172.4
	tert → *tert*	
C7 ⇌ C6m3	isom B	176.7
	sec → *sec*	
C7 ⇌ C6m2	isom B	178.4
	sec → *sec*	
C6m2 ⇌ C5m2m3	isom B	179.0
	tert → *tert*	
C5m2m4 ⇌ C4m2m2m3	isom B	179.2
	tert → *tert*	
C6m2 ⇌ C5m2m4	isom B	181.0
	sec → *sec*	
C6m3 ⇌ C5m3m3	isom B	183.7
	tert → *sec*	
C6m2 ⇌ C5m2m2	isom B	192.2
	tert → *sec*	
C5m2m4 → iC4 + C3	cracking B2	173.2
C5m2m2 → iC4 + C3	cracking B1	182.7
C5m3m3 → iC5 + C2	cracking D	188.7
C5m2m3 → nC4 + C3	cracking C	188.8
C5e3 → nC5 + C2	cracking D	192.1
C6m2 → nC4 + C3	cracking C	201.6
nC5 → C3 + C2	cracking D	202.2
C6m3 → nC4 + C3	cracking C	204.4
C7 → nC4 + C3	cracking D	206.5
iC5 → C3 + C2	cracking E	210.5
C4m2m2m3 → iC4 + C3	cracking E	239.1

[a] For the reverse reaction C5m2m3 → C5m2m2.

Table 3
Fitted kinetic constants (Pre-exponential factors at 500 K and overall activity multiplier for the different feeds) optimized over all datasets including runs for *n*-heptane, 2-methylhexane and 2,2-dimethylpentane hydroconversion over zeolite BEA.

Reaction Type	Pre-exponential factors at 500 K (s^{-1})
C7 isomerization	$2.377 \cdot 10^{14}$
Cracking of C7	$2.065 \cdot 10^{15}$
Cracking of C5	$8.655 \cdot 10^{15}$
Experiment runs (feed)	**Overall activity multiplier relative to *n*-heptane**
2-methylhexane	0.98
2,2-dimethylpentane	0.63

precursor carbenium ion being tertiary and the (formal) product ion being secondary. Indeed, a similar value of 166 kJ/mol was calculated for the analogous reaction of C5m2m3 to C5m2m2, which is the reverse reaction of the first entry of Table 2. The barrier for formation of the ethyl isomer (C6m3 to C5e3), an ethyl shift reaction, is at 170 kJ/mol slightly higher than that of the other type A isomerization reactions.

Type B isomerization reactions are found to all have higher activation enthalpies than type A isomerization reactions. They lie in a narrow range of 172–181 kJ/mol, except for the reactions forming geminal dimethyl isomers, *i.e.* isomerization of 3-methylhexane (C6m3) to 3,3-dimethylpentane (C5m3m3) and of 2-methylhexane (C6m2) to 2,2-dimethylpentane (C5m2m2) which have higher activation enthalpies still, of 184 and 192 kJ/mol, respectively. Again, reactions forming geminal dimethyl isomers formally involve conversion of tertiary carbenium ions to secondary carbenium ions. As mentioned, the higher barriers for type B isomerization are explained by a higher energy closed-primary meso-PCP transition state [43,44]. It is worth summarizing the above by noting that, except for the ethyl shift reaction, within each isomerization class the fitted values for activation enthalpies appear to follow the order, in terms of carbenium ions formally involved:

sec → *tert* < *sec* → *sec* ∼ *tert* → *tert* < *tert* → *sec*

with the qualification that *tert* → *tert* type A isomerizations do not occur in the C7 network (except C4m2m2m3 ⇌ C4m2m2m3).

Type B1 and B2 cracking reactions of 2,2-dimethylpentane (C5m2m2) and 2,4-dimethylpentane (C5m2m4) are found to have activation enthalpies of 183 and 173 kJ/mol, respectively, in the same range as that for type B isomerization reactions.

Type C cracking reactions have higher activation enthalpies with cracking of monomethyl isomers (C6m2 and C6m3) being slower than cracking of 2,3-dimethylpentane ($\Delta H^{\ddagger}$ of 202, 204 and 189 kJ/mol respectively). Type D/E cracking reactions are slowest with activation enthalpies ranging from 190 to 240 kJ/mol, as expected. They also have minimal impact on the reaction network and are included to allow formation of small amounts of pentane and isopentane cracking products which are formed by type D cracking of 3-ethyl-pentane (C5e3) and 3,3-dimethylpentane (C5m3m3) respectively.

The pre-factors due to entropic changes for formation of activated transition state (from Table 3) are about an order of magnitude higher for cracking reactions compared to isomerization reactions. They are also about four times higher for C5 cracking reactions compared to C7 cracking reactions. As expressed through the activity multipliers, it was necessary to assume a lower catalyst activity by a factor of 0.63 for the 2,2-dimethylpentane run compared to the *n*-hexane feed run. There is no definite explanation for this lower activity, but the simplest explanation would be that 2,2-dimethylpentane, which had a lower purity than the other feeds, contained a small feed impurity causing overall inhibition, such as a trace alkene or oxygenate. We did not seek further clarification of this aspect.

In Figs. 5, 6 and 7 we plot the comparison of simulated molar concentrations at the outlet of the reactor with experimentally measured molar concentrations (expressed as fraction of the total) from hydroconversion experiments conducted at the highest catalyst loading of 300 mg and varying temperatures for feed of *n*-heptane (GHSV = 81.6 Nml/g/min), 2-methyl-hexane (GHSV = 75.7 Nml/g/min) and 2,2-dimethylpentane (GHSV = 72.8 Nml/g/min) respectively. The trends of various isomerization and cracking products match very well with the experimental data obtained from different temperature runs for both n-heptane and 2-methylpentane feed runs. For experiments with 2,2-dimethylpentane feed all components show consistent trends with experimental data. We observe a higher conversion of 2,2-dimethylpentane to various isomers at lower temperatures (below 500 K) compared to simulated runs. This disagreement between the simulated and experimentally observed concentration of various isomers at low temperature is apparent in profiles plotted in Fig. 7, however the cracking products such as iC4 and C3 show consistently good agreement between simulations and experiments. That the fits somewhat underestimate isomerization of 2,2-dimethylpentane at the low temperature end (470–500 K) could be due to an overestimation of the corresponding activation energies which in turn might result from the simplifying assumption

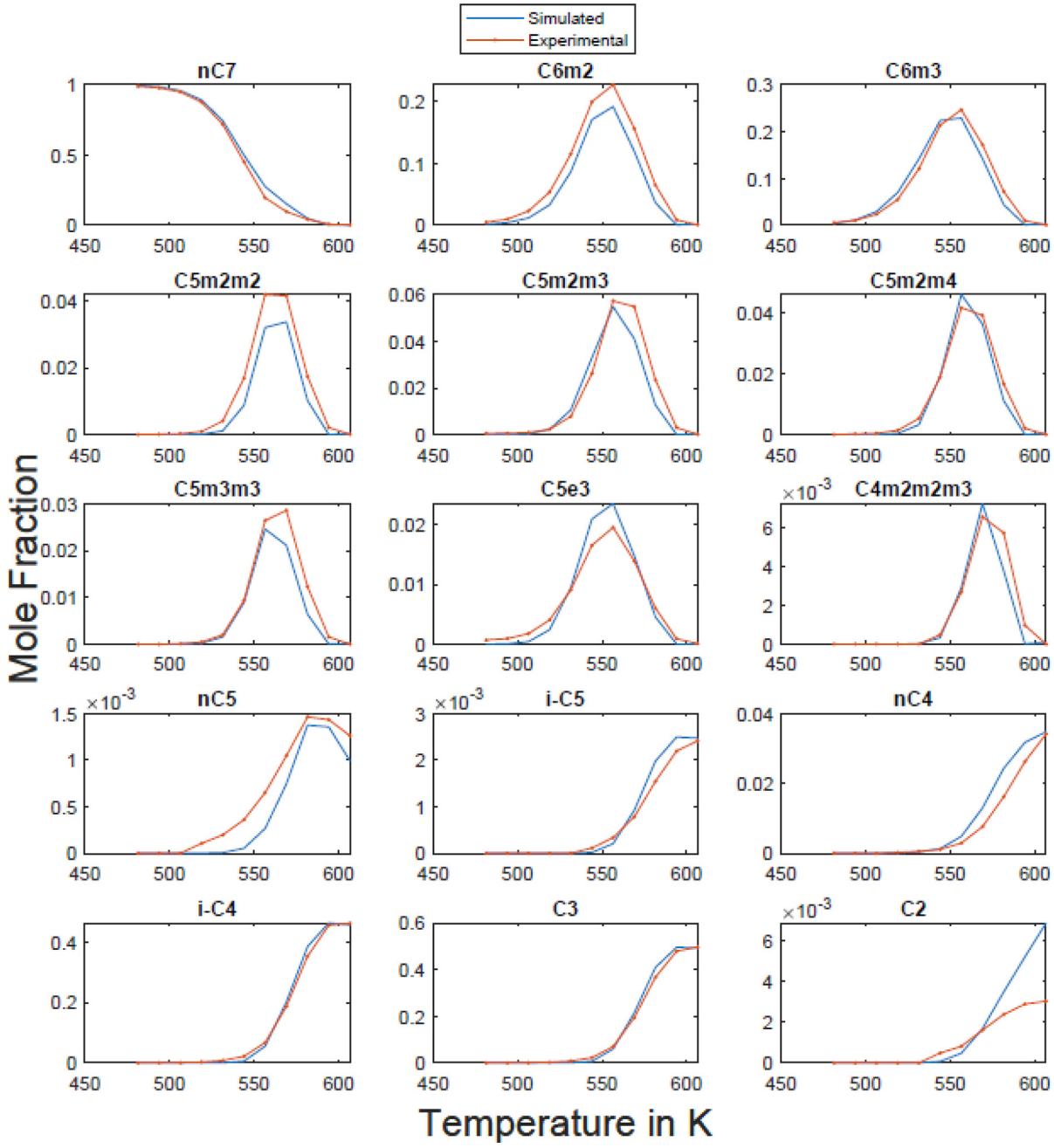

Fig. 5. Normalized molar concentration (mole fraction, as mol/mol total hydrocarbons) of different components at the outlet of the reactor, experimental (in red) and simulation (in blue) for *n*-heptane as feedstock as a function of reaction temperature (in Kelvin) for catalyst loading of 300 mg (GHSV of 81.6 Nml/g/min). (For interpretation of the references to colour in this figure legend, the reader is referred to the web version of this article.)

(required to limit the number of degrees of freedom) to equate pre-exponential factors for similar reactions.

Comparison of kinetic parameters in this work with literature data requires some assumptions in each case. For hydroconversion of C_9 to C_{15} alkanes over zeolites PtCaY [50] and PtHZSM-5 [46] Weitkamp et al. found effective activation energies at low conversion close to 190 kJ/mol, which is in reasonable agreement with the 177–178 kJ/mol reported here for the initial branching reactions of *n*-heptane. The assumption allowing a direct comparison of these numbers is that the literature results have been obtained in a saturated pore regime, which seems reasonable under the conditions used (e.g., for *n*-tridecane: p_{nC13} = 14 kPa, T = 473–493 K).

We find that type B isomerization reactions have higher barriers than type A isomerization reactions, as expected, but only by about 12–22 kJ/mol. Similarly, the single event kinetic model for *n*-C_{16} hydroisomerization over zeolite Beta [11] yields only modestly higher barriers for type B isomerization compared to type A isomerization by 16 to 32 kJ/mol, when expressed as effective alkene-to-alkene barriers, *i.e.*, $\Delta H_{prot} + E_{act}$ from Table 1 of Ref. [11]. In contrast, Rey et al. [12,44] have calculated by means of periodic DFT activation enthalpies of 67 kJ/mol for the type B isomerization of 2,4-dimethylpent-2-enium to 2,3,3-trimethylbut-2-enium and ~15 kJ/mol for the type A methyl shift in 2,3,3-trimethylbut-2-enium, both in zeolite Chabazite; and hence a much higher difference of 52 kJ/mol. Smaller differences were more recently reported for other type B isomerizations [12]. Comparison of absolute values for the barriers is more difficult, as it depends heavily on assumptions, such as the value of the enthalpy

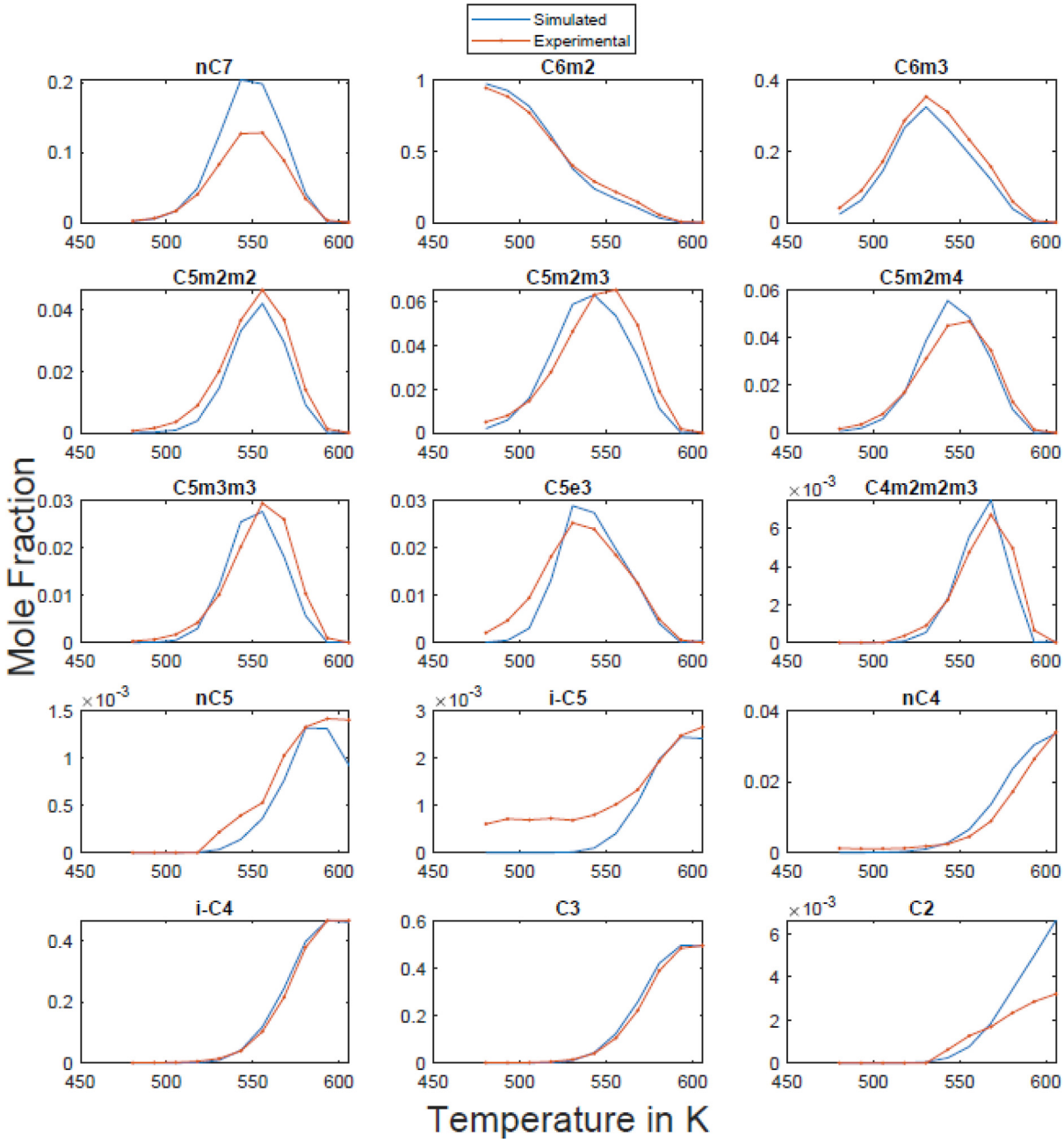

Fig. 6. Normalized molar concentration (mole fraction, as mol/mol total hydrocarbons) of different components at the outlet of the reactor, experimental (in red) and simulation (in blue) for 2-methylhexane as feedstock as a function of reaction temperature (in Kelvin) for catalyst loading of 300 mg (GHSV of 75.7 Nml/g/min). (For interpretation of the references to colour in this figure legend, the reader is referred to the web version of this article.)

of protonation of a physisorbed alkene (see also Fig. 1). As an example, from the DFT ion-to-ion barrier for type A isomerization of 15 kJ/mol, an overall isoalkane-to-isoalkane barrier in the order of 173 kJ/mol may be estimated by adding + 110 kJ/mol for the enthalpy of dehydrogenation [51] and + 48 kJ/mol for the enthalpy of protonation of a physiosorbed alkene [33], with which our values for the barriers of type A isomerization of 161–170 kJ/mol are in reasonable agreement.

The optimized reactor model can subsequently be used for further analysis of the hydroconversion process. In Fig. 8, we plot results from a hydroconversion simulation conducted at 594 K and 300 mg catalyst loading for *n*-heptane feed. For runs at this reaction temperature full conversion to cracking products is achieved, and 80% *n*-heptane conversion is reached already at 20% of the reactor length. The plot of mole fraction of various isomers vs. n-C_7 conversion (Fig. 8, right) illustrates the sequence of product formation, via monobranched to dibranched and finally tribranched species. Primary isomerization product 3-methylhexane subsequently isomerizes into 2,3-dimethylpentane and 3-ethylpentane respectively and the other primary isomerization product, 2-methylhexane, also isomerizes predominantly into 2,3-dimethylpentane. Isomerization of 2,3-dimethyl-pentane to 2,4-dimethylpentane at intermediate conversions and geminal dibranched isomers such as 2,2-dimethylpentane and 3,3-dimethylpentane at higher conversions is also observed from the plot. Formation of 2,2-dimethylpentane and 3,3-dimethylpentane is limited and occurs at only higher conversion due to enthalpic penalty associated with formation of these geminal di-branched

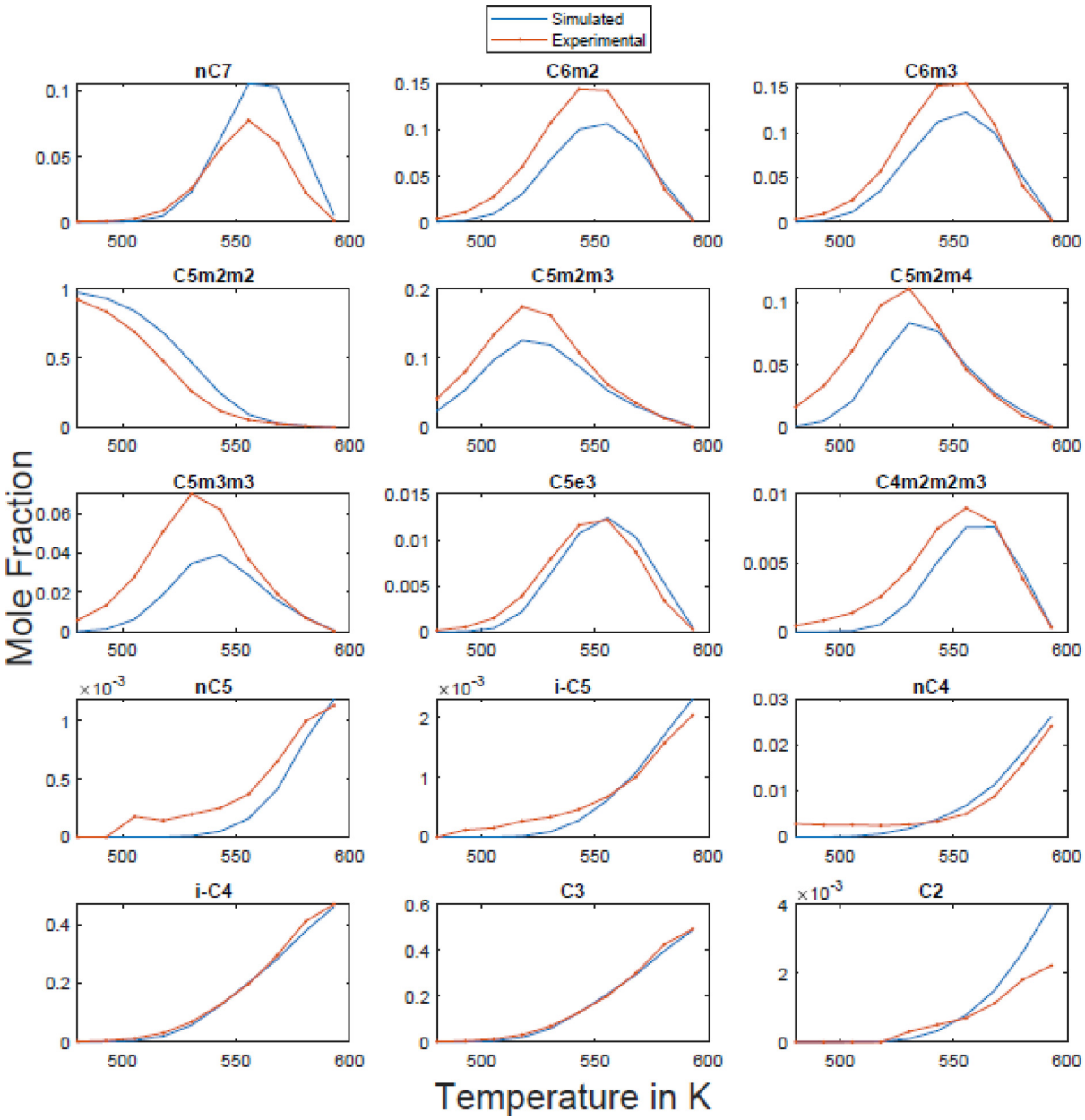

Fig. 7. Normalized molar concentration (mole fraction) of different components at the the outlet of the reactor, experimental (in red) and simulation (in blue) for 2,2-dimethylpentane as feedstock as a function of reaction temperature (in kelvin) for catalyst loading of 300 mg (GHSV of 72.8 Nml/g/min). (For interpretation of the references to colour in this figure legend, the reader is referred to the web version of this article.)

isomers. Similarly, 2,2,3-trimethyl-butane which has highest activation enthalpy for formation of transition state is formed only at high conversion of n-heptane (peak at around 90% heptane conversion) and in very low quantities.

Due to large pore sizes of zeolite Beta (~6.5 Å), no diffusion limitation for transport of any of the dibranched isomers is expected. As a limited verification, *n*-heptane hydroconversion experiments were performed for samples of different primary crystal sizes and compared, and indeed no indications for diffusion limitation were found (see supporting information). Although some preferential adsorption occurs among heptane isomers, none are spatially restricted, and the preference is not very strong. Hence, equilibrium among isomers is established relatively quickly after each step of the sequence has set in. Once 2,3-dimethylpentane is formed via Type B isomerization of 2/3-methylhexane isomers, relatively fast type A isomerization (methyl shift) reactions establish and maintain the relative equilibrium concentrations for all the dibranched isomers. Based on the reaction network illustrated in Fig. 4 cracking of 2,3-dimethyl-pentane proceeds via type C cracking with a higher free energy barrier compared to type B1 and B2 cracking of 2,2-dimethyl-pentane and 2,4-dimethyl-pentane. Hence, cracking of 2,3-dimethylpentane is slower compared to that of 2,4-dimethylpentane and 2,2-dimethylpentane. To maintain the dynamical equilibrium between all dibranched isomers, a faster cracking of 2,4 dimethylpentane would lead to increased isomerization of 2,3-dimethyl pentane (and any other dibranched isomer) to 2,4-dimethylpentane. To verify this, in Fig. 9 we plot the net integral rates of various isomerization and cracking reactions by tracking all the forward and reverse reaction rates and calculating net rates for each node of the reactor bed at 594 K and 300 mg catalyst loading. Based on this information we can determine how the entire hydroconversion process occurs. As observed in Fig. 9 (top),

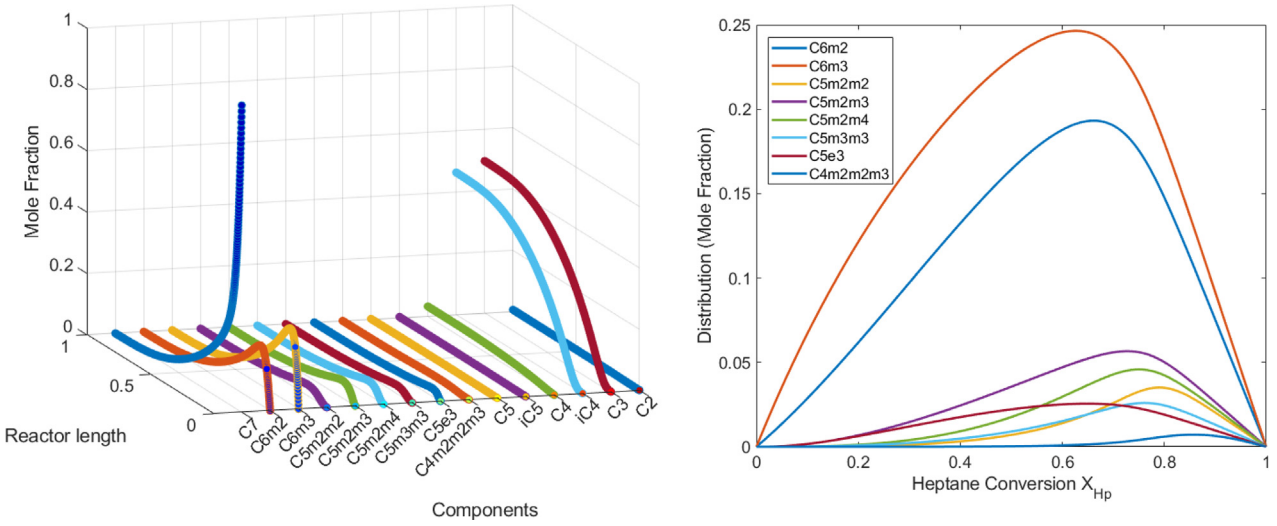

Fig. 8. Left: Normalized molar concentration (mol per mol of C_7 feed) of different components plotted as a function of the reactor length with n-heptane feedstock. Right: Normalized molar concentration (mol per mol of C_7 feed) of various n-heptane isomers as a function of heptane conversion for simulations conducted at 594 K.

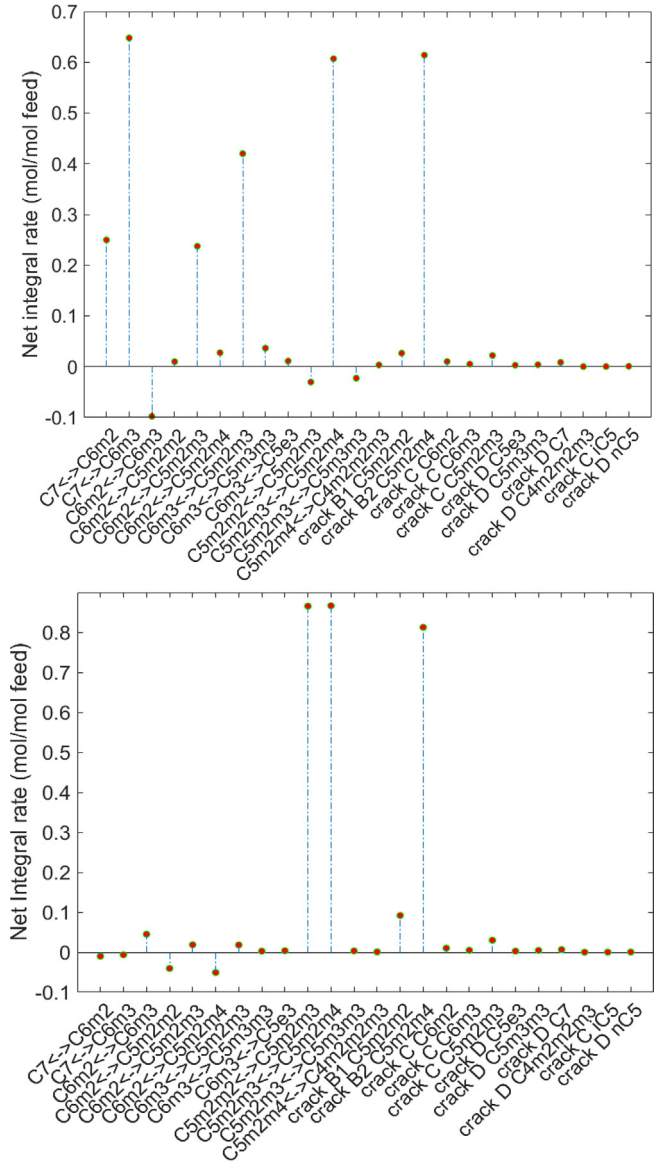

Fig. 9. Integrated net rates, expressed as mol converted per mol of feed, of various reversible isomerization and irreversible cracking reactions for simulations conducted at 594 K for n-heptane (top) and 2,2-dimethylpentane (bottom) feedstock.

the dominant pathway for hydroisomerization and hydrocracking in a large pore zeolite such as Beta zeolite for n-heptane feedstock is n-heptane → 2/3-methylhexane → 2,3-dimethylpentane → 2,4-dimethylpentane → isobutane + propane. The dominant cracking reaction is therefore a type B2 cracking reaction. Similarly, based on the net integral rates for 2,2-dimethylpentane feed simulations, the dominant pathway for conversion is 2,2-dimethylpentane → 2,3-dimethylpentane → 2,4-dimethylpentane → isobutane + propane. Other isomerization reactions help maintain the equilibrium distribution for all the isomers and form cracking products in relatively smaller concentration in agreement with experimentally observed concentrations. The other competing pathway is type B1 cracking of 2,2-dimethyl-pentane which contributes minimally, in part due to delayed and limited formation of 2,2-dimethylpentane for *n*-heptane feed. For 2,2-dimethylpentane feed it contributes more, however the type A isomerization to other isomers such as 2,3-dimethylpentane is still preferred over direct cracking of 2,2-dimethylpentane. In terms of the carbenium ion formalism, type B2 cracking via tertiary 2,4-dimethylpent-2-enium to secondary 2-propenium is apparently faster than type B1 cracking via secondary 4,4-dimethylpent-2-enium to a *tert*-butyl cation and propene. Static DFT and ab initio MD calculations yielded the same order for analogous octene isomers in H-ZSM-5 [34,35].

4. Conclusions

A reactor model that deconvolutes thermodynamics of adsorption of hydrocarbon in the pores of zeolite Beta, obtained by Configurational-Bias Monte Carlo simulations, from intrinsic, intraporous kinetics of hydroisomerization and hydrocracking reactions, provides a good quantitative description of all significant reactions in the kinetic network for interconversion and cracking of different heptane isomers. Activation enthalpies obtained for those intraporous reactions follow the expected order according to the carbenium ion formalism:

methyl shift < ethyl shift < isom(B) ∼ crack(B2) < crack(B1) < crack(C) ∼ crack(D) < crack(E)

and apparently within each isomerization class, in terms of carbenium ions formally involved:

sec → *tert* < *sec* → *sec* ∼ *tert* → *tert* < *tert* → *sec*

except for the ethyl shift reaction forming 3-ethylpentane.

In zeolite Beta, cracking happens primarily through 2,4-dimethylpentane, by the type B2 mechanism, regardless of the initial reactant. Type B1 cracking of 2,2-dimethylpentane also occurs but to a much lesser extent even from 2,2-dimethylpentane feed, due to its higher activation enthalpy. The model can subsequently be used to separate the effect of pore structure on selective adsorption and on intraporous reaction kinetics, and zeolite Beta will serve as a base case for a comparison of different zeolite structures.

Data availability

Data will be made available on request.

Declaration of Competing Interest

The authors declare that they have no known competing financial interests or personal relationships that could have appeared to influence the work reported in this paper.

Acknowledgements

TJHV acknowledges NWO-CW for a VICI grant. This work was sponsored by NWO Domain Science for the use of supercomputer facilities. This work is part of the Advanced Research Center for Chemical Building Blocks, ARC-CBBC, which is co-funded and co-financed by the Netherlands Organization for Scientific Research (NWO) and the Netherlands Ministry of Economic Affairs and Climate Policy.

Appendix A. Supplementary data

Supplementary data to this article can be found online at https://doi.org/10.1016/j.jcat.2022.09.026.

References

[1] J.A.R. van Veen, J.K. Minderhoud, L.G. Huve, W.H.J. Stork, Hydrocracking and Catalytic Dewaxing, in: Handbook of Heterogeneous Catalysis, Wiley-VCH Verlag GmbH & Co. KGaA, 2008.
[2] B. Smit, T.L.M. Maesen, Towards a molecular understanding of shape selectivity, Nature 451 (7179) (2008) 671–678.
[3] T.L.M. Maesen, M. Schenk, T.J.H. Vlugt, J.P. de Jonge, B. Smit, The Shape Selectivity of Paraffin Hydroconversion on TON-, MTT-, and AEL-Type Sieves, J. Catal. 188 (2) (1999) 403–412.
[4] J.A. Martens, P.A. Jacobs, The potential and limitations of the n-decane hydroconversion as a test reaction for characterization of the void space of molecular sieve zeolites, Zeolites 6 (5) (1986) 334–348.
[5] W. Haag, N. Chen, Catalyst design with zeolites, Catalyst Design: Progress and Perspectives, (1987) 163–212.
[6] A. Poursaeidesfahani, M.F. de Lange, F. Khodadadian, D. Dubbeldam, M. Rigutto, N. Nair, T.J.H. Vlugt, Product shape selectivity of MFI-type, MEL-type, and BEA-type zeolites in the catalytic hydroconversion of heptane, J. Catal. 353 (2017) 54–62.
[7] J. Oenema, J. Harmel, R.P. Vélez, M.J. Meijerink, W. Eijsvogel, A. Poursaeidesfahani, T.J.H. Vlugt, J. Zečević, K.P. de Jong, Influence of Nanoscale Intimacy and Zeolite Micropore Size on the Performance of Bifunctional Catalysts for n-Heptane Hydroisomerization, ACS Catal. 10 (23) (2020) 14245–14257.
[8] J. Weitkamp, Catalytic Hydrocracking—Mechanisms and Versatility of the Process, ChemCatChem 4 (3) (2012) 292–306.
[9] G.D. Svoboda, E. Vynckier, B. Debrabandere, G.F. Froment, Single-Event Rate Parameters for Paraffin Hydrocracking on a Pt/US-Y Zeolite, Ind. Eng. Chem. Res. 34 (11) (1995) 3793–3800.
[10] G.G. Martens, G.B. Marin, J.A. Martens, P.A. Jacobs, G.V. Baron, A Fundamental Kinetic Model for Hydrocracking of C8 to C12 Alkanes on Pt/US–Y Zeolites, J. Catal. 195 (2) (2000) 253–267.
[11] B.D. Vandegehuchte, J.W. Thybaut, A. Martínez, M.A. Arribas, G.B. Marin, n-Hexadecane hydrocracking Single-Event MicroKinetics on Pt/H-beta, Appl. Catal. A 441–442 (2012) 10–20.
[12] J.-M. Schweitzer, J. Rey, C. Bignaud, T. Bučko, P. Raybaud, M. Moscovici-Mirande, F. Portejoie, C. James, C. Bouchy, C. Chizallet, Multiscale Modeling as a Tool for the Prediction of Catalytic Performances: The Case of n-Heptane Hydroconversion in a Large-Pore Zeolite, ACS Catal. (2022) 1068–1081.
[13] I.R. Choudhury, K. Hayasaka, J.W. Thybaut, C.S. Laxmi Narasimhan, J.F. Denayer, J.A. Martens, G.B. Marin, Pt/H-ZSM-22 hydroisomerization catalysts optimization guided by Single-Event MicroKinetic modeling, J. Catal. 290 (2012) 165–176.
[14] E.J.M. Hensen, D.G. Poduval, D.A.J.M. Ligthart, J.A.R. van Veen, M.S. Rigutto, Quantification of Strong Bronsted Acid Sites in Aluminosilicates, J. Phys. Chem. C 114 (2010) 8363–8374.
[15] F. Regali, M. Boutonnet, S. Järås, Hydrocracking of n-hexadecane on noble metal/silica–alumina catalysts, Catal. Today 214 (2013) 12–18.
[16] D. Dubbeldam, S. Calero, D.E. Ellis, R.Q. Snurr, RASPA: molecular simulation software for adsorption and diffusion in flexible nanoporous materials, Mol. Simul. 42 (2016) 81–101.
[17] D. Dubbeldam, A. Torres-Knoop, K.S. Walton, On the inner workings of Monte Carlo codes, Mol. Simul. 39 (2013) 1253–1292.
[18] T.J.H. Vlugt, R. Krishna, B. Smit, Molecular Simulations of Adsorption Isotherms for Linear and Branched Alkanes and Their Mixtures in Silicalite, J. Phys. Chem. B 103 (1999) 1102–1118.
[19] J.I. Siepmann, D. Frenkel, Configurational bias Monte Carlo: a new sampling scheme for flexible chains, Mol. Phys. 75 (1992) 59–70.
[20] M. Laso, J.J. de Pablo, U.W. Suter, Simulation of phase equilibria for chain molecules, J. Chem. Phys. 97 (1992) 2817–2819.
[21] J. Houdayer, The wormhole move: A new algorithm for polymer simulations, J. Chem. Phys. 116 (2002) 1783–1787.
[22] J.I. Siepmann, A method for the direct calculation of chemical potentials for dense chain systems, Mol. Phys. 70 (1990) 1145–1158.
[23] J.I. Siepmann, S. Karaborni, B. Smit, Vapor-liquid equilibria of model alkanes, J. Am. Chem. Soc. 115 (1993) 6454–6455.
[24] J.J. Potoff, J.I. Siepmann, Vapor–liquid equilibria of mixtures containing alkanes, carbon dioxide, and nitrogen, AIChE J. 47 (2001) 1676–1682.
[25] M.G. Martin, J.I. Siepmann, Transferable Potentials for Phase Equilibria. 1. United-Atom Description of n-Alkanes, J. Phys. Chem. B 102 (1998) 2569–2577.
[26] P. Bai, M. Tsapatsis, J.I. Siepmann, TraPPE-zeo: Transferable Potentials for Phase Equilibria Force Field for All-Silica Zeolites, J. Phys. Chem. C 117 (2013) 24375–24387.
[27] C. Baerlocher, L.B. McCusker, Database of Zeolite Structures: http://www.iza-structure.org/databases/, International Zeolite Association and Structure Commission.
[28] T.J.H. Vlugt, M. Schenk, Influence of Framework Flexibility on the Adsorption Properties of Hydrocarbons in the Zeolite Silicalite, J. Phys. Chem. B 106 (2002) 12757–12763.
[29] B. Widom, Some Topics in the Theory of Fluids, J. Chem. Phys. 39 (1963) 2808–2812.
[30] T.J.H. Vlugt, E. García-Pérez, D. Dubbeldam, S. Ban, S. Calero, Computing the Heat of Adsorption using Molecular Simulations: The Effect of Strong Coulombic Interactions, J. Chem. Theory Comput. 4 (7) (2008) 1107–1118.
[31] J.A. Martens, P.A. Jacobs, Conceptual Background for the Conversion of Hydrocarbons on Heterogeneous Acid Catalysts, in: Theoretical Aspects of Heterogeneous Catalysis, Springer Netherlands, Dordrecht, 1990, pp. 52–109.
[32] M. Steijns, G. Froment, P. Jacobs, J. Uytterhaeven, J. Weitkamp, Hydroisomerization and hydrocracking. 2. Product distributions from n-decane and n-dodecane, Ind. Eng. Chem. Prod. Res. Dev. 20 (4) (1981) 654–660.
[33] Q. Ren, M. Rybicki, J. Sauer, Interaction of C3–C5 Alkenes with Zeolitic Brønsted Sites: π-Complexes, Alkoxides, and Carbenium Ions in H-FER, J. Phys. Chem. C 124 (18) (2020) 10067–10078.
[34] M.N. Mazar, S. Al-Hashimi, M. Cococcioni, A. Bhan, β-Scission of Olefins on Acidic Zeolites: A Periodic PBE-D Study in H-ZSM-5, J. Phys. Chem. C 117 (45) (2013) 23609–23620.
[35] P. Cnudde, K. De Wispelaere, L. Vanduyfhuys, R. Demuynck, J. Van der Mynsbrugge, M. Waroquier, V. Van Speybroeck, How Chain Length and Branching Influence the Alkene Cracking Reactivity on H-ZSM-5, ACS Catal. 8 (10) (2018) 9579–9595.
[36] P.B. Weisz, Polyfunctional Heterogeneous Catalysis, in: D.D. Eley, P.W. Selwood, P.B. Weisz, A.A. Balandin, J.H. De Boer, P.J. Debye, P.H. Emmett, J. Horiuti, W. Jost, G. Natta, E.K. Rideal, H.S. Taylor (Eds.), Advances in Catalysis, Academic Press, 1962, pp. 137–190.
[37] H.L. Coonradt, W.E. Garwood, Mechanism of Hydrocracking. Reactions of Paraffins and Olefins, Ind. Eng. Chem. Process Design Develop. 3 (1) (1964) 38–45.
[38] J. Weitkamp, S. Ernst, P. Jacobs, H. Karge, Erdoel, Kohle, Erdgas, Petrochem, Brennst. Chem 31 (1978) 13.
[39] D.M. Brouwer, J.M. Oelderik, HF-SbF5 catalysed isomerization of 2-methylpentane: Kinetics and mechanism of rearrangement and hydride-ion transfer steps in alkylcarbonium ion reactions, Recl. Trav. Chim. Pays-Bas 87 (6) (1968) 721–736.
[40] M. Saunders, S.P. Budiansky, Computer modelling of multi-step carbonium ion rearrangements: Applications to methylcyclopentyl and t-amyl, Tetrahedron 35 (8) (1979) 929–932.
[41] F. Ribeiro, C. Marcilly, M. Guisnet, Hydroisomerization of n-hexane on platinum zeolites: I. Kinetic study of the reaction on platinum/Y-zeolite catalysts: Influence of the platinum content, J. Catal. 78 (1982) 267–274.
[42] D.M. Brouwer, H. Hogeveen, Electrophilic Substitutions at Alkanes and in Alkylcarbonium Ions, in: Progress in Physical Organic Chemistry, John Wiley & Sons, Inc., 2007, pp. 179–240.

[43] D.J.S. Sandbeck, D.J. Markewich, A.L.L. East, The Carbocation Rearrangement Mechanism, Clarified, J. Org. Chem. 81 (4) (2016) 1410–1415.
[44] J. Rey, A. Gomez, P. Raybaud, C. Chizallet, T. Bučko, On the origin of the difference between type A and type B skeletal isomerization of alkenes catalyzed by zeolites: The crucial input of ab initio molecular dynamics, J. Catal. 373 (2019) 361–373.
[45] J. Rey, P. Raybaud, C. Chizallet, T. Bučko, Competition of Secondary versus Tertiary Carbenium Routes for the Type B Isomerization of Alkenes over Acid Zeolites Quantified by Ab Initio Molecular Dynamics Simulations, ACS Catal. 9 (11) (2019) 9813–9828.
[46] J. Weitkamp, P.A. Jacobs, J.A. Martens, Isomerization and hydrocracking of C9 through C16 n-alkanes on Pt/HZSM-5 zeolite, Appl. Catal. 8 (1) (1983) 123–141.
[47] J.S. Buchanan, J.G. Santiesteban, W.O. Haag, Mechanistic Considerations in Acid-Catalyzed Cracking of Olefins, J. Catal. 158 (1) (1996) 279–287.
[48] K.J. Laidler, M.C. King, Development of transition-state theory, J. Phys. Chem. 87 (15) (1983) 2657–2664.
[49] D.W. Scott, Chemical Thermodynamic Properties of Hydrocarbons and Related Substances: Properties of the Alkane Hydrocarbons, C1 through C10, in the Ideal Gas State From 0 to 1500 K, US Department of the Interior, Bureau of Mines, 1974.
[50] J. Weitkamp, Isomerization of long-chain n-alkanes on a Pt/CaY zeolite catalyst, Ind. Eng. Chem. Prod. Res. Dev. 21 (4) (1982) 550–558.
[51] D.W. Rogers, K. Dejroongruang, Enthalpies of hydrogenation of the dimethylpentenes, ethylpentenes, methylethylbutene, and trimethylbutene, J. Chem. Thermodyn. 21 (1989) 1115–1120.